Journal of
Composites Science

MDPI

Article

Impact of $CoFe_2O_4$ Magnetic Nanoparticles on the Physical and Mechanical Properties and Shape Memory Effect of Polylactide

Anna Zimina [1,*], Aleksey Nikitin [1], Vladislav Lvov [1], Inna Bulygina [1], Polina Kovaleva [1], Stepan Vodopyanov [1], Mikhail Zadorozhnyy [1], Elizaveta Peshkina [1], Saida Karshieva [1,2], Rajan Choudhary [3,4], Maxim Abakumov [1] and Fedor Senatov [1]

[1] Institute of Biomedical Engineering, National University of Science and Technology "MISIS", 119049 Moscow, Russia; nikitin.chemistry@mail.ru (A.N.); lvov.va@misis.ru (V.L.); ibulygina@misis.ru (I.B.); zhukova.pa@yandex.ru (P.K.); stepan.vodopianov@yandex.ru (S.V.); priboy38@mail.ru (M.Z.); m1909880@edu.misis.ru (E.P.); skarshieva@gmail.com (S.K.); abakumov.ma@misis.ru (M.A.); senatov@misis.ru (F.S.)
[2] N.N. Blokhin National Medical Research Center of Oncology, 115478 Moscow, Russia
[3] Rudolfs Cimdins Riga Biomaterials Innovations and Development Centre, Institute of General Chemical Engineering, Faculty of Materials Science and Applied Chemistry, Riga Technical University, Pulka St 3, LV-1007 Riga, Latvia; rajandeshwal@gmail.com
[4] Baltic Biomaterials Centre of Excellence, Riga Technical University, Kipsala Street 6A, LV-1048 Riga, Latvia
* Correspondence: a.zimina@misis.ru

Abstract: The acceleration in advancements of smart materials and non-contact controlled devices in the field of 4D printing is facilitated by the use of magnetically responsive shape memory polymer (SMP) composites. This study is dedicated to the development of promising shape memory materials based on polylactic acid (PLA) and cobalt ferrite ($CoFe_2O_4$) nanoparticles. The activation of the shape memory effect (SME) in magnetic nanoparticle composites was achieved by applying a high-frequency alternating magnetic field (HFAMF). The PLA/$CoFe_2O_4$ composites exhibited a remarkable shape recovery ratio (>84%) and underwent rapid heating when exposed to HFAMF. The interaction of these composites with mouse adipose-derived mesenchymal stem cells demonstrated adequate cytocompatibility. The rapid magnetosensitive behavior and high shape recovery characteristics of PLA/$CoFe_2O_4$ composites make them promising candidates for biomedical applications.

Keywords: polylactide; $CoFe_2O_4$ nanoparticles; shape memory effect; magneto-responsive composites; smart materials

Citation: Zimina, A.; Nikitin, A.; Lvov, V.; Bulygina, I.; Kovaleva, P.; Vodopyanov, S.; Zadorozhnyy, M.; Peshkina, E.; Karshieva, S.; Choudhary, R.; et al. Impact of $CoFe_2O_4$ Magnetic Nanoparticles on the Physical and Mechanical Properties and Shape Memory Effect of Polylactide. *J. Compos. Sci.* **2024**, *8*, 48. https://doi.org/10.3390/jcs8020048

Academic Editor: Francesco Tornabene

Received: 15 November 2023
Revised: 15 January 2024
Accepted: 24 January 2024
Published: 27 January 2024

1. Introduction

Polymeric materials are extensively used in various biomedical applications such as drug delivery systems, tissue engineering scaffolds, hydrogels, biodegradable sutures, wound dressings etc. [1]. The field of biomedical polymers continues to advance, with the development of novel and smart materials [2–5]. Shape memory polymers (SMPs) are "smart" materials that can restore their original shape from a deformed shape when exposed to an external stimulus [6,7]. Owing to versatility and low cost, SMPs are used to fabricate orthopedic devices [8], vascular stents [9], orthodontic wire for brackets [10], craniofacial meshes and plates [11], and neural probes [12].

SMPs are gaining popularity in the development of medical devices particularly for minimally invasive surgical procedures. For example, a compressed medical device can be introduced into a living system through a small incision, which later transforms into its intended shape under the influence of a suitable trigger. Thermally activated polymers are the most common SMPs [13]. In addition to direct heating, indirect heating methods have also been developed due to the concerns associated with the overheating of surrounding tissues. For instance, SMPs with functional fillers can be activated by light [14–17], electricity [18–20], magnetic fields [21–23], or microwaves [24,25], but in fact

they are still activated by heat since different forms of energy can be converted to heat through the functional fillers. However, indirect triggers such as exposure to solvent [26,27], ultrasound [28,29], and other triggers [30–32] have also been reported.

The parameters governing the shape memory effect in polymers can be controlled by incorporating particles; altering composition; physical properties such as thermal transitions and degree of crystallinity; and processing or programming conditions [33]. In semicrystalline polymers, a shift in shape is induced by heating it above the glass transition temperature (T_g) [34], or above the melting transition of crystalline domain [35]. Programming the shape of SMPs is possible by increasing the mobility of molecular segments when heated above the transition temperature. The characteristics of the SME depend on the material's structure, particularly the coexistence of hard and soft phases, which determines the entropy elasticity of macromolecules [36,37]. Crystalline regions serve as "nodes" facilitating the recovery of the original shape. However, the extent of their presence can both enhance and limit the shape memory effect.

Hyperthermia is a medical cancer treatment that involves raising the temperature of the body to 41–46 °C [38]. During this treatment process both healthy and tumor tissues are affected. Nanoparticle-induced hyperthermia gained popularity for localizing treatment. Magnetic nanoparticles (MNPs) have potential to convert the electromagnetic energy of HFAMF into thermal energy [39]. MNPs-based hyperthermia is a clinically approved method for treating cancer [40]. These MNPs can be magnetic alloy nanoparticles (MANPs), such as Fe–Ni, Co–Pt, etc., or magnetic metal oxide nanoparticles (MMONPs), such as Fe_3O_4, $MnFe_2O_4$, and $CoFe_2O_4$ [41].

In the biomedical field, magnetically activated shape memory polymer composites have shown considerable promising results. Unlike methods requiring direct heating, these materials can be remotely controlled, enhancing safety and facilitating minimally invasive insertion of medical devices [42]. When exposed to an external HFAMF, magnetic particles within the material undergo induction heating. This internal heating of shape memory polymer triggers the shape memory effect when activation temperature is reached [43–45].

Polylactide (PLA) is a thermoplastic aliphatic polyester widely used in biomedicine due to its biocompatibility and bioresorption ability [46,47]. PLA exhibits a distinct shape memory effect, which becomes evident at the glass transition temperature (T_g = 55–65 °C). This process occurs as the polymer transitions into a viscoelastic state [48–50]. The addition of a filler into a polymer alters the transition temperature and shape memory characteristics, as the inclusions form new nodes in the molecular structure of the polymer matrix. For example, incorporation of inorganic additives (TiO_2 [51], carbon nanotubes [52], Al_2O_3 [53], and SiO_2 [54]) in a PLA matrix not only mitigates the drawbacks of pure PLA but also enhances its overall properties.

Cobalt ferrite ($CoFe_2O_4$) MNPs are of particular interest for magnetic hyperthermia due to their large cubic magneto-crystalline anisotropy and high coercivity value [55]. Ferrite nanomaterials with a spinel structure, including cobalt-spinel ferrite, possess high saturation magnetization, high permeability, and no preferred direction of magnetization as compared to widely studied iron oxides [56]. In addition, $CoFe_2O_4$ NPs exhibit high anisotropy and slower relaxation time than iron oxide nanoparticles. These characteristics make $CoFe_2O_4$ NPs a good alternative for the treatment of hyperthermia [57]. MNPs of $CoFe_2O_4$ are extensively used in magnetic hyperthermia imaging, magnetic separation, biosensors, and drug delivery [58–62], due to their excellent physical and chemical properties and absence of cytotoxicity in therapeutic concentration [63]. The stability of these particles in the physiological environment was studied by coating the surface of $CoFe_2O_4$ MNPs with organic moieties such as citric or olein acid [64].

The objectives of this work are to develop a cytocompatible, magnetically activated SMP having enhanced heating speed and a high recovery rate. Additionally, we also aimed to ensure the 3D printing feasibility of SMP. The $CoFe_2O_4$ nanoparticles synthesized by coprecipitation, and the structure and morphology, as well as magnetic properties of the nanoparticles was studied. A detailed analysis of the thermal, structural, and mechanical properties of the composite material and the impact of different concentrations

of $CoFe_2O_4$ nanoparticles on them was performed. Moreover, the heating rate and recovery coefficient of the deformed samples' shape under the influence of a magnetic field were measured. Finally, the cytocompatability of composites in contact with mouse adipose-derived mesenchymal stem cells was also evaluated.

2. Materials and Methods

2.1. Materials

Polylactide (molecular weight of 110 kg/mol) was received from Nature Works LLC (Plymouth, MN, USA). Earlier investigations on the shape memory effect involved the use of similar polylactide samples [50,65,66]. Prior to experiments, the PLA pellets were dried at 60 °C for 6 h in a hot air oven.

Synthesis of $CoFe_2O_4$ Nanoparticles (NPs)

Cobalt ferrite nanoparticles were obtained by coprecipitation. This method is simple to implement and makes it possible to obtain a high yield of nanoparticles stable in aqueous medium. To obtain NPs at the first stage, 1.62 g of iron (III) chloride ($FeCl_3$, ≥98%, Sigma-Aldrich, St. Louis, MO, USA) was dissolved in 20 mL of deionized water. A solution of 2.15 g of cobalt chloride hexahydrate ($CoCl_2$-$6H_2O$, 98%, Plasmotherm, Moscow, Russia) in 2 mL of deionized water (Milli-Q water) and 0.5 mL of hydrochloric acid (HCl, 36%, Sigma-Tek, Augusta, KS, USA) was added to the obtained solution. The obtained solution was stirred on a magnetic stirrer for several minutes and added dropwise to 100 mL of 1 M sodium hydroxide solution (NaOH, ≥98%, Sigma-Aldrich), preheated to boiling point. The boiling solution was maintained for 30 min with continuous vigorous stirring of the reaction mixture. After 30 min, the reaction mixture was cooled, the nanoparticles were separated from the solution with a permanent magnet, and washed with deionized water (3 times 100 mL each). Next, 315 mL of 2 M nitric acid (HNO_3, 65%, Sigma-Aldrich) was added to the resulting precipitate of NPs, as well as a solution of 1.27 g of iron nitrate ($Fe(NO_3)_3$, ≥98%, Reactivetorg, Moscow, Russia) in 15 mL of deionized water. The resulting solution was brought to a boil and held under vigorous stirring for 1 h. After that, the reaction mixture was cooled to room temperature, the NPs were separated from the solution using a permanent magnet and washed with 2 M HNO_3 solution (3 times 100 mL each). The resulting precipitate of NPs was redispersed in 50 mL of deionized water. In the second step, 10 mL of 0.2 M citric acid ($C_6H_8O_7$, 98%, Sigma-Aldrich) solution was added to 50 mL of NPs solution, after which the pH of the solution was adjusted to 7.4 using 1 M NaOH solution. To get rid of the excess of citrate ions uncoordinated on the surface of $CoFe_2O_4$, the obtained nanoparticle solution was washed using centrifuge filters [67].

2.2. Characterization of $CoFe_2O_4$ NPs

2.2.1. Transmission Electron Microscopy

Transmission electron microscopy (TEM) images were acquired with a Titan Themis Z (Thermo Fisher Scientific, Landsmeer, The Netherlands) transmission electron microscope equipped with a DCOR+ condenser system spherical aberration corrector at an accelerating voltage of 200 kV. The average NPs size was estimated from more than 300 particles in semi-automated mode using ImageJ software (version 1.53t).

2.2.2. X-ray Diffraction

The phase composition of the NPs was studied via X-ray diffraction (XRD) analysis using a DRON-4 (Burevestnik, Russia) diffractometer with Co K_α radiation. The experimental points were recorded in the range of angles 2θ = 20–100° at a scanning speed of 0.1° in one step.

2.2.3. Study of Magnetic Properties

The magnetic properties of the cobalt ferrite nanoparticle samples (saturation specific magnetization (J_S), residual specific magnetization (J_R), and coercivity (H_C)) were

investigated at room temperature in the Physical Property Measurement System (PPMS) DynaCool (Quantum Design, San-Diego, CA, USA) with the option of vibration magnetometry. Dry nanoparticle powders were prepared for recording magnetic hysteresis loops. The specific magnetization of each sample was calculated from the iron concentration measured by atomic emission spectroscopy (AES).

2.3. Composite Material Preparation Technique

Cobalt ferrite nanoparticles (1, 5, and 10 wt.%) were used as inorganic fillers in a polylactide matrix for the fabrication of composites. These composites were prepared by extrusion using a rheological extrusion twin-screw microcompounder HAAKE MiniLab II (Thermo Fisher Scientific, Waltham, MA, USA). Screw speed, chamber heating temperature, and dwell time was optimized to ensure uniform mixing and to minimize defects during the extrusion process. This method was used to produce filaments for 3D printing with a diameter of 1.7 ± 0.2 mm, as well as ribbons with a width of 3.1 ± 0.2 mm and a thickness of 1.2 ± 0.2 mm.

2.4. 3D Printing

A three-dimensional model of specimens was designed using SolidWorks 2021 software (Dassault Systèmes, Vélizy-Villacoublay, France), which represents a parallelepiped with dimensions of $10 \times 6 \times 12$ mm, with subsequent conversion of the model into G-code with pre-defined settings using PrusaSlicer 2.6.1 software (Prusa Research, Prague, Czech Republic). The samples were 3D printed by fused deposition modeling using BiZon Prusa i3 Steel PRO (3DiY, Moscow, Russia). Extruder temperature was kept at 180 °C, table temperature was maintained 60 °C, and the extruder nozzle height was 0.6 mm with a printing speed of 5 mm/s and 100% filling density. The filling type used in these experiments was concentric.

2.5. Characterization of Composite Materials

2.5.1. Differential Scanning Calorimetry

The thermal properties of the materials were studied by differential scanning calorimetry (DSC) using a DSC 204 F1 calorimeter (Netzsch GmbH & Co. KG, Selb, Germany). The following mode was used: heating from 30 to 210 °C, holding at 210 °C for 10 min, cooling to 30 °C, holding for 10 min, and reheating to 210 °C. The heating and cooling rates were 10 °C/min. The tests were performed in an argon atmosphere (50 mL/min). The degree of crystallinity (χ) was calculated according to Equation (1) as follows:

$$\chi = \frac{\Delta H_m - \Delta H_{cc}}{\Delta H_m^{100\%} \cdot \omega_{PLA}} \quad (1)$$

where ΔH_m is the melting enthalpy and ΔH_{cc} is the cold crystallization enthalpy.

$\Delta {H_m}^{100\%}$ is the theoretical melting enthalpy of 100% crystalline PLA, which was 93 J/g [68]; ω is the mass fraction of PLA in the composite.

2.5.2. Shape Memory Effect Parameters

Parameters of the shape memory effect, such as restoring stress and restoring strain, were investigated using a dynamic mechanical analyzer DMA Q800 (TA Instruments, New Castle, DE, USA). The measurement was performed in the temperature range of 26–80 °C at a heating rate of 2 °C/min. The samples were stretched by 100% in length and tested to evaluate the recovery stress and recovery strain. In the first case, the specimens were clamped on both sides to determine the recovery stress. In the second case, one of the grips was movable to evaluate the change in specimen length. The test was performed on ribbon samples ($30 \times 5 \times 1$ mm).

2.5.3. Study of Mechanical Properties

The compressive strength, in particular Young's modulus, of a series of 3D-printed $10 \times 6 \times 12$ mm specimens with different percentages of $CoFe_2O_4$ in PLA were investigated using a Zwick/Roell Z020 universal testing machine (Zwick GmbH & Co. KG, Ulm, Germany). The test was performed at a speed of 1 mm/min until complete failure of the specimens was observed.

2.5.4. SME Activation in a High-Frequency Alternating Magnetic Field

The composite samples (1, 5, 10 wt.%, n = 5 for each composition) were placed in the cuvette of a TOR UltraHT (Nanomaterials LLC, Tambov, Russia) high-frequency alternating magnetic field generator to investigate the activation of the shape memory effect in the magnetic field, as well as to measure the heating rate and the degree of shape recovery. Heating was performed at the magnetic field amplitude H = 9.6 kA·m^{-1} and frequency f = 261 kHz. The temperature of the samples was measured with a Seek Thermal camera having an accuracy of $\pm 0.1^{\circ}$. Heating rate graphs were plotted by recording the temperature after every second, followed by initiation of exposure to HFAMF.

All samples were deformed by 20% in height before being loaded into the cuvette. The height of the samples before deformation, after deformation, and after recovery in the magnetic field were measured with a caliper. The degree of shape recovery of the samples was counted as the ratio of the height after recovery to the height before deformation.

The SME of the fabricated composite was studied in contact with a mouse small intestine model to assess its potential biomedical application. 3D-printed PLA/$CoFe_2O_4$ (5 wt.%) clips in the shape of a not fully closing ring were preliminary deformed, and a small intestine was placed in the center of the clip. The proposed model was designed based on the size and shape of the small intestine; the outer and inner diameter were 6 and 1 mm, respectively, and the height was 2 mm. The system was placed into the cuvette of the HFAMF generator (magnetic field amplitude H = 9.6 kA·m^{-1} and frequency f = 261 kHz). The experiment was recorded with a Seek Thermal camera, and samples before and after the exposure to magnetic field were photographed.

2.6. In Vitro Studies

2.6.1. MSC Isolation from Mice Adipose Tissue and Culture

Mouse adipose-derived mesenchymal stem cells (mAD-MSC) were isolated from the subcutaneous adipose tissue of Balb/c mice. Adipose tissue was cut into fine pieces and digested with 0.2% collagenase IA (PanEco, Moscow, Russia) for 40 min at 37 °C with shaking at a speed of 200 rpm. The cell suspension was then washed twice in PBS and filtered through a 100 mm nylon filter. Cells were pelleted by centrifugation at $279\times g$ for 20 min and then were resuspended and cultured in DMEM/low glucose (1 g/L, PanEco), supplemented with 10% FBS (HiMedia, Maharashtra, India), 2 mM L-glutamine (PanEco), antibiotic-antimycotic mix (Biosera, Cholet, France), and incubated at 37 °C in 5% CO_2 atmosphere. For all experimental procedures we used early passage (P3–P4) mAD-MSCs. The mAD-MSC were characterized by the expression of mesenchymal markers and the ability to differentiate into adipogenic and osteogenic cell lines, as described earlier [69].

2.6.2. MTS-Test

The MTS test to evaluate the cytotoxicity of the samples was performed on mouse adipose-derived mesenchymal stem cell culture (mAD-MSC). This standard in vitro test shows whether the samples under study affect the proliferative activity of the cells. This procedure as well as the SME study on the mouse's small intestine was conducted with the approval of the Local Ethical Committee of the N.N. Blokhin NMRC of Oncology (document no. Act708n dated 23.08.2010), Moscow, Russia.

The mAD-MSC cells thawed from liquid nitrogen (p6 passaging) were seeded into DMEM/F12 medium supplemented with 10% fetal bovine serum (FBS) and 2 mM glutamine in culture flasks (T25), and grown under standard conditions (37 °C, 5% CO_2).

When 80–90% confluence of the monolayer was achieved, cells were transferred to a new flask in fresh cell culture medium.

The PLA samples without NPs and with cobalt ferrite NPs (1, 5, and 10 wt.%) for the cytotoxicity test were ribbons about 3 mm width and about 1 mm thickness. Such ribbons were cut into rectangular pieces of 3 mm by 4 mm to fit easily into the bottom of the well of a 96-well plate. The samples were then sterilized by immersing them in 70% ethanol for 15 min, dried under sterile conditions, and placed at the bottom of the 96-well plate wells. Each sample was tested in six replicates. An amount of 10,000 mAD-MSC cells in cell culture medium were seeded into the wells on top of the sample pieces. Samples were not placed in control wells; here, cells were seeded directly at the bottom of the wells. The cells were incubated with samples and in control wells for 24 h under standard conditions. Light microscopy was used to check whether the cells had seeded the surface of the samples after 24 h of incubation.

Further, the cell culture medium in the wells was replaced with the medium with the MTS reagent and incubated for 4 h under standard conditions. Additionally, blanks (wells without cells filled with medium and reagent) were placed on the plate in order to subtract the optical density of the medium with reagent without cells from the optical density values in the measured wells. The medium with the reaction products from the measured wells and blank wells was transferred (saving the scheme of the experiment) to another clear plate so that the PLA samples would not interfere with the optical density measurement in the wells. The measurement was carried out on a MultiScan GO (Thermo Fisher Scientific, USA) spectrophotometer at a wavelength of 490 nm.

The calculation of the proportion of surviving cells (A, %) in the well relative to the control was carried out according to Equation (2) as follows:

$$A = \frac{OD_w - \overline{OD_b}}{\overline{OD_c} - \overline{OD_b}} \cdot 100\% \quad (2)$$

where OD_w—the optical density of experimental well; $\overline{OD_b}$—the average optical density of the blanks wells; and $\overline{OD_c}$—the optical density of control wells.

2.7. Statistical Analysis

Statistical data were analyzed, and graphs were plotted using OriginPro software (version 10.0.5.157, Originlab Corporation, Northampton, MA, USA) and reported as Mean ± SD. Statistical significance for mechanical testing results was determined at $p < 0.05$. Most of the experiments were repeated at least three times independently.

3. Results and Discussion

3.1. Study of the Structure and Morphology of $CoFe_2O_4$ NPs

Synthesized $CoFe_2O_4$ NPs were characterized by means of TEM and XRD. As can be seen in Figure S1, NPs are polydispersed and do not have a distinct morphology. The average size of the magnetic cores of NPs determined using the ImageJ software was 11 ± 3 nm. The coprecipitation method is used to obtain nanoparticles based on iron oxide (including cobalt ferrites). This method makes it possible to obtain nanoparticles in a shorter time. This approach has become widespread due to its simplicity and economy. In addition, it makes it possible to obtain a large number of nanoparticles; therefore, it is widely used by many researchers to obtain cobalt nanoferrites [70].

X-ray diffraction analysis of the $CoFe_2O_4$ NPs sample is presented in Table S1 and Figure S2. The lattice parameter value a = 8.370 Å is consistent with the lattice parameter of bulk cobalt ferrite a = 8.377 ($CoFe_2O_4$, ICDD No.22-1086). Comparison of the size of $CoFe_2O_4$ NPs, determined from X-ray diffraction analysis and TEM, indicates a single-crystal nature.

3.2. Study of the Magnetic Properties of $CoFe_2O_4$ NPs

It is known that the magnetic moment in ferrites comes mainly from the proportional, uncompensated intrinsic spin of an individual ion. Therefore, the probability of magnetization is explained by considering the distribution of metal ions and the antiparallel alignment of spins at two sites of the sublattice. According to the Neel model, of the three types of interactions A-A, A-B, and B-B, the intersublattice A-B superexchange interaction is the most appropriate. The net magnetization is thus the solution of the vector sum of the magnetization of the two sublattices, i.e., $J_S = J_B - J_A$, where J_A and J_B are the magnetizations of sublattices A and B, respectively.

Figure S3 shows the magnetization curves of cobalt ferrite MNPs. According to the results of magnetometry, it was found that for the obtained MNPs $J_S = 75$ A·m^2·kg^{-1}, which is close to that for the bulk material ($J_S = 80$ A·m^2·kg^{-1}) [57]. The values of the residual magnetization and coercive force were $J_R = 4$ A·m^2·kg^{-1} and $H_C = 3$ kA·m^{-1}, respectively, which indicates the ferromagnetic nature of MNPs and, as in the case of $CoFe_2O_4$ samples, is consistent with the previously established critical grain size (6–8 nm), below which $CoFe_2O_4$ passes into the superparamagnetic state [71].

3.3. Differential Scanning Calorimetry

SME in polymers is determined by phase transitions. In the case of PLA, the glass transition temperature (T_g) serves as the switching temperature, causing the chain segments' mobility to become severely limited [72,73]. The melting-crystallization behavior of PLA/$CoFe_2O_4$ composites were evaluated by DSC. DSC curves are presented in Figure 1, and the main thermal parameters, including glass transition temperature (T_g), cold crystallization temperature (T_{cc}), T_m, and χ, are summarized in Table 1.

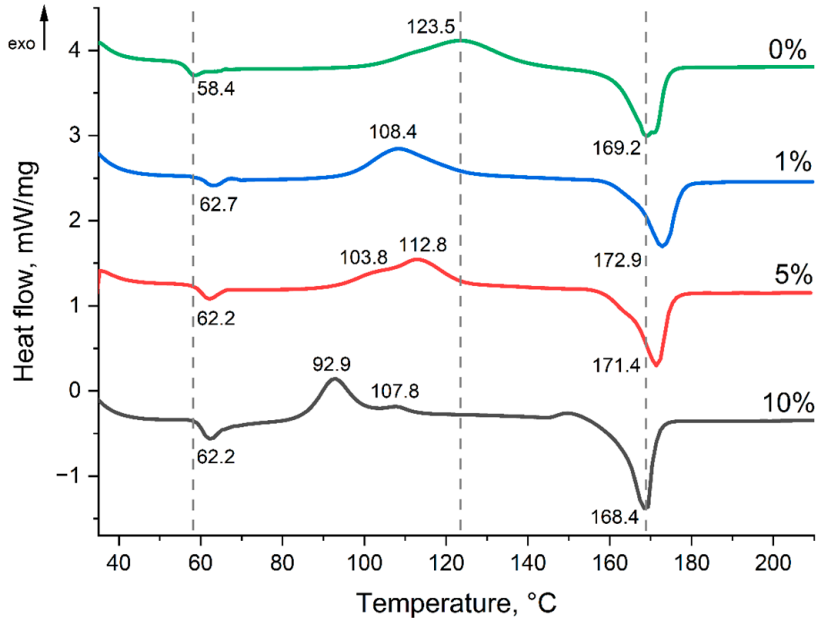

Figure 1. DSC curves of PLA and PLA/$CoFe_2O_4$ samples.

Table 1. T_g, T_{cc}, T_m and degree of crystallinity for PLA and PLA/$CoFe_2O_4$ samples.

$CoFe_2O_4$ Mass Fraction, %	T_g, °C	T_{cc}, °C	T_m, °C	χ
0	58.4	123.5	169.2	1.6
1	62.7	108.4	172.9	7.6
5	62.2	103.8, 112.8	171.4	8.1
10	62.2	92.9, 107.8	168.4	27.0

As shown in Table 1, T_g of the extruded specimens increases with the addition of $CoFe_2O_4$ NPs from 58.4 °C for pure PLA, to 62.2 °C and 62.7 °C for composites. Chain mobility, intermolecular interactions, and molecular weight are important factors that affect T_g. The values of the T_{cc} shifted to lower values, which is probably because lamellar crystals formed during the cooling process. In addition, curves for composites with 5% and 10 wt.% of $CoFe_2O_4$ NPs revealed the second peak of cold crystallization. Cold crystallization phenomena are characteristic of amorphous or partially crystallized polymers when heated above the glass transition temperature; however, a double cold crystallization peak is observed in DSC curves infrequently. The double peak of cold crystallization may mean crystallization from interlamellar and interspherolitic amorphous regions controlled by the degree of nucleation and diffusion. Interlamellar amorphous regions, consisting of chain folds, chain ends, and linking chains, have some order compared to completely amorphous interspherolitic regions, so they crystallize at a lower temperature. With the dominance of nucleation (high supercooling and crystallization from the glassy state), more interlamellar amorphous regions are formed than interspherolitic. On the other hand, if diffusion prevails (weak supercooling, crystallization from the melt), more interspherolitic amorphous regions can be expected than interlamellar ones [74].

The addition of $CoFe_2O_4$ NPs had a strong effect on heterogeneous nucleation and significantly enhanced the crystallization of PLA chains. In addition, according to the calculation using Equation (1), the degree of crystallinity was only 1.6% for pure PLA. The degree of crystallinity increased significantly, up to 27.0%, with the content of $CoFe_2O_4$ NPs at 10 wt.%. PLA has low melt crystallinity due to rigid chains, and most PLA chains reorganize during the thermal cycle [75].

3.4. Parameters of the Shape Memory Effect

Figure S4 shows the deformation curves during reshaping. The temperature at the beginning of the recoverable deformation decreased with an increase in the mass fraction of $CoFe_2O_4$ NPs in the PLA matrix. Thus, for pure PLA, the temperature was 61.7 °C, and for a sample containing 10 wt.% of cobalt ferrite, the temperature decreased to 59.5 °C.

The reactive stress curves are shown in Figure 2. The stress curve shows a drop towards negative values, which reflects the relaxation process during heating. Further, after a certain temperature, the stresses began to increase sharply. To estimate the restoring stresses, the change in stress after relaxation to the maximum value was calculated. The results are presented in Table 2. The analysis showed that there was no strong change in the value of reactive stresses; their values increased from 3.0 MPa for pure PLA to 3.6 MPa for the PLA/$CoFe_2O_4$ composite (10 wt.%). With an increase in the proportion of filler, the reactive stresses increased, probably due to an increase in the "hard" crystalline phase in the polymer. There were also no strong changes in the temperature values at which the stresses began to increase; the temperature rose with the addition of 1% and 5 wt.% $CoFe_2O_4$ NPs from 53.7 °C (for pure PLA) to 54.1 °C, and with a weight fraction of $CoFe_2O_4$ NPs of 10%, this temperature decreased to 52.8 °C. This temperature can be considered the starting temperature of the shape memory effect.

Table 2. Recovery stress variation and SME activation temperature of PLA and PLA/$CoFe_2O_4$ samples.

Weight Fraction of $CoFe_2O_4$, wt.%	**0**	**1**	**5**	**10**
Recovery stress variation, MPa	3.0	3.2	3.5	3.6
Activation temperature of SME, °C	53.7	54.1	54.1	52.8

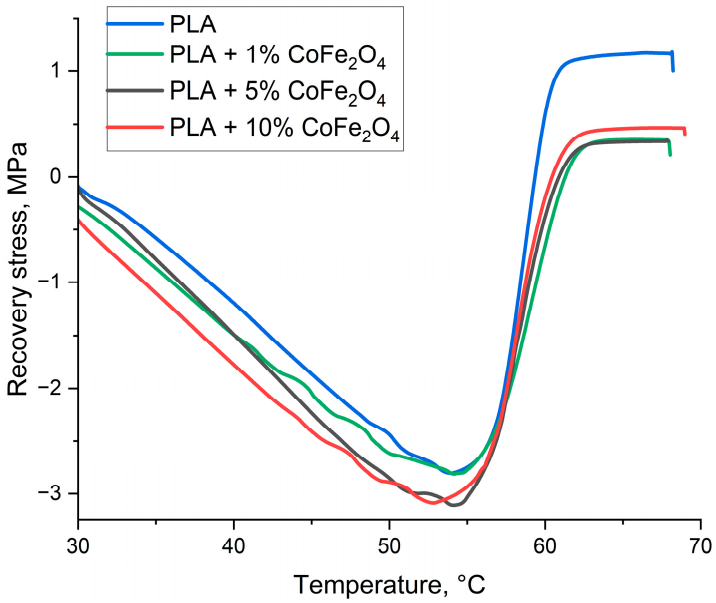

Figure 2. Recovery stress curves for PLA and PLA/$CoFe_2O_4$ (1, 5, 10 wt.%) samples.

3.5. Study of Mechanical Properties

The introduction of $CoFe_2O_4$ particles into PLA promotes crystallization of the polymer around the particles, which leads to a decrease in Young's modulus of the samples by almost 1.5 times (Figure 3, Table 3). Similarly, when the concentration of $CoFe_2O_4$ particles increases from 1% to 10%, the number of crystallinity zones increases and the strength of the material decreases, as evidenced by the graph in Figure 3.

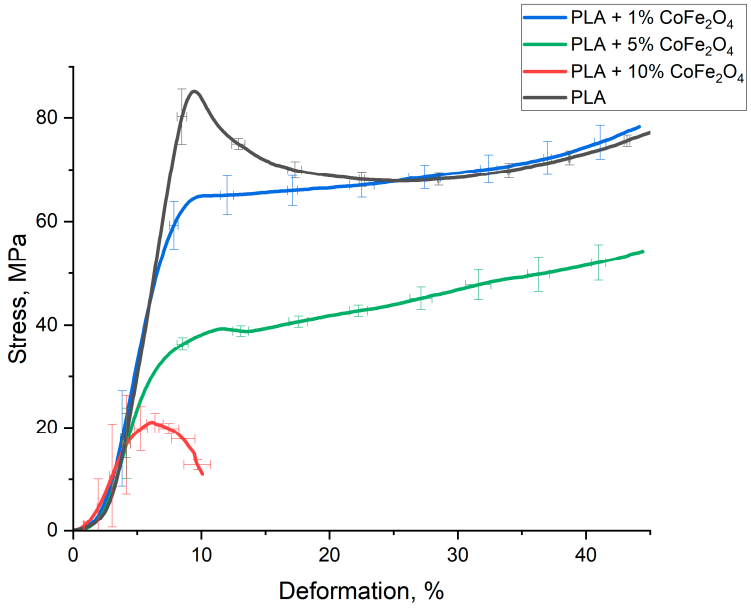

Figure 3. Compression curves for PLA and PLA/$CoFe_2O_4$ (1, 5, 10 wt.%) samples.

Table 3. Elastic modulus of PLA and PLA/$CoFe_2O_4$ samples.

Weight Fraction of $CoFe_2O_4$, wt.%	Elastic Modulus, MPa
0	1201 ± 12
1	1205 ± 21
5	914 ± 97
10	760 ± 23

3.6. SME Activation in a High-Frequency Alternating Magnetic Field

The graph presented in Figure 4 clearly shows the dependence of the heating rate on the amount of filler in the composite material. Composite material with 1 wt.% of $CoFe_2O_4$ heated the slowest of all—in 300 s it heated up by about 10 °C; SME activation temperature was not reached. PLA/$CoFe_2O_4$ (5 wt.%) showed an average heating rate—in 300 s the material heated up by more than 75 °C; the activation temperature was reached in 100 s. The composite material with 10 wt.% of $CoFe_2O_4$ heated up the fastest—in about 120 s it reached the melting point (168.4 °C); the activation temperature was reached in 35 s.

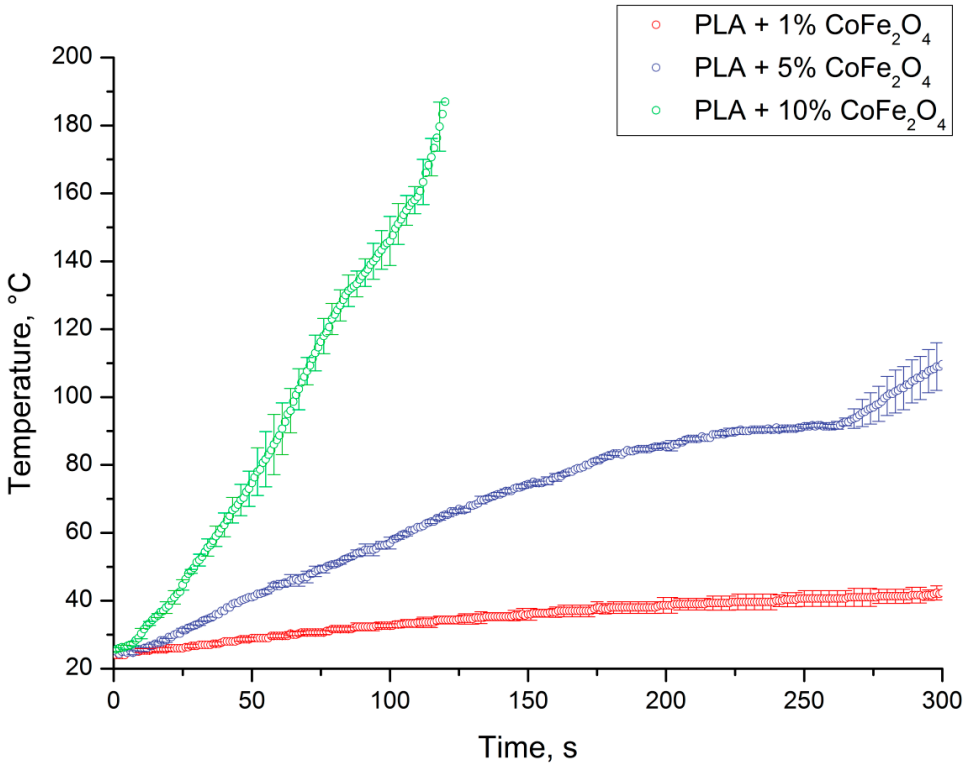

Figure 4. Heating rate in a high-frequency alternating magnetic field (H = 9.6 kA·m^{-1}, f = 261 kHz) curves for PLA/$CoFe_2O_4$ (1, 5, 10 wt.%) samples.

The height values of the samples before deformation, after deformation, and after shape recovery in a high-frequency alternating magnetic field are shown in Figure 5. All types of samples, regardless of the amount of filler, restore their shape. The values of the shape recovery coefficient, which is equal to the ratio of the height of the samples after restoration to the original height, are shown in Figure 6 and Table 4. The shape recovery is best demonstrated by samples of the composite material with 5 wt.% of $CoFe_2O_4$—the recovery coefficient of this material is 94.06%. PLA/$CoFe_2O_4$ (1 wt.%) composite material recovers its shape worse than PLA/$CoFe_2O_4$ (5 wt.%) and has a recovery rate of 84.89%. This is in good agreement with the DSC results and the values of the degree of crystallinity.

Table 4. Recovery coefficient of PLA/$CoFe_2O_4$ (1, 5, 10 wt.%) samples.

Weight Fraction of $CoFe_2O_4$, wt.%	Recovery Coefficient, %
1	84.89 ± 1.33
5	94.06 ± 0.47
10	93.82 ± 0.58

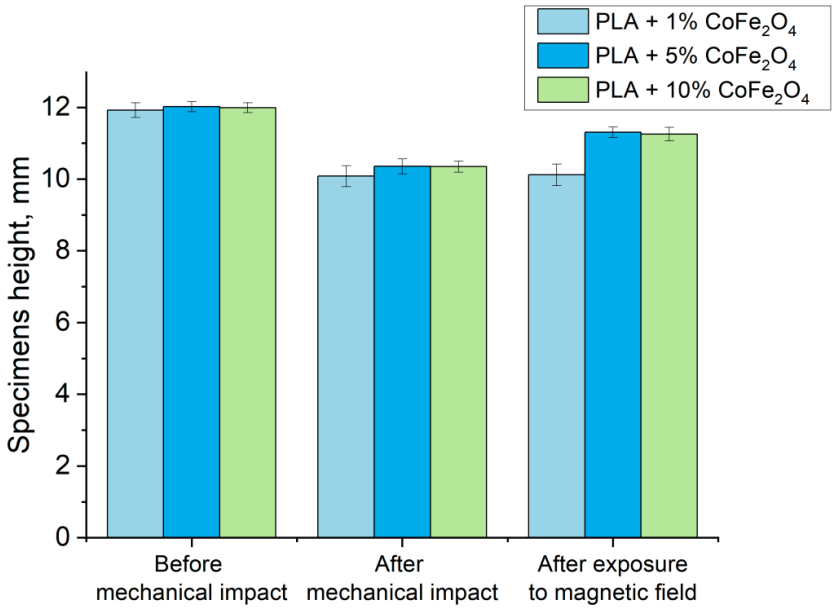

Figure 5. Height values of PLA/$CoFe_2O_4$ (1, 5, 10 wt.%) samples before deformation, after deformation, and after shape recovery in a high-frequency alternating magnetic field (H = 9.6 kA·m^{-1}, f = 261 kHz).

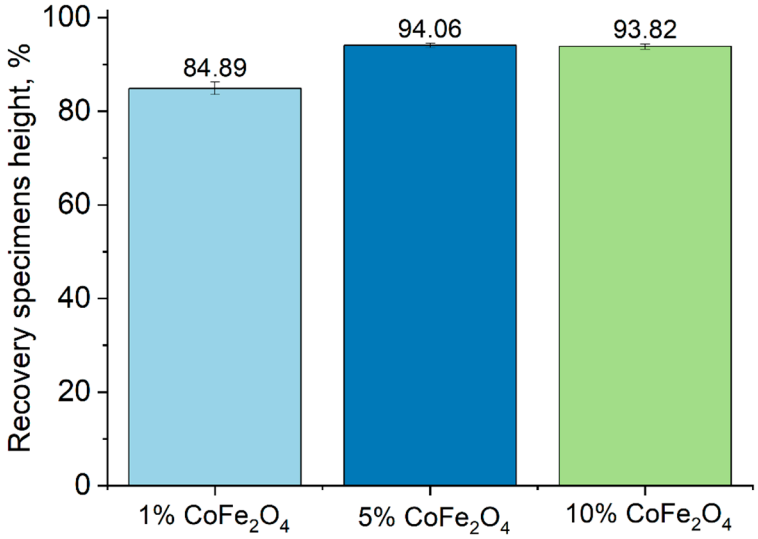

Figure 6. Recovery coefficient of PLA/$CoFe_2O_4$ (1, 5, 10 wt.%) samples after exposure to a high-frequency alternating magnetic field (H = 9.6 kA·m^{-1}, f = 261 kHz).

The greater the amount of filler in the polymer composite material, the higher the degree of crystallinity of the polymer matrix. This is due to the fact that the filler particles act as crystallization centers. In turn, crystalline zones, such as nodes of the polymer molecular network or filler particles, are the elements responsible for fixing the "permanent" shape and its restoration after deformation. However, as can be seen in Figure 6, a sample with a mass fraction of $CoFe_2O_4$ NPs of 10% recovers shape worse (the recovery coefficient is 93.82%) than a sample with a mass fraction of $CoFe_2O_4$ NPs of 5%. This is due to the fact that the formation of a large number of network nodes impedes the movement of a free molecular chain, which leads to a decrease in the recovery factor [73].

The shape recovery of the clip in HFAMF in the presence of the mouse's small intestine is demonstrated in Video S1 and Figure S5. The permeability of the mouse's small intestine was demonstrated by injection of PBS from syringe through the central hole. After that, intestine was inserted into the ring-shaped clip and subjected to the HFAMF. The tempera-

ture change during indirect heating of the PLA/$CoFe_2O_4$ clip was recorded, showing the achievement of the SME activation temperature, and thus proving the possibility of soft tissue compression by the proposed biomedical material-based device. The compressed clip blocked fluid flow through the intestine due to HMAMF exposure.

3.7. In Vitro Experiment

Light microscopy made it possible to detect cells only on samples of PLA and PLA + 1% $CoFe_2O_4$ (Figures S6 and S7). Cells could not be seen on the surface of samples with 5 and 10% $CoFe_2O_4$ NPs in transmitted light because the samples turned black due to the addition of NPs.

The results of the cytotoxicity evaluation are presented in Table 5 and Figure 7. The proportion of viable cells in the wells with all samples was practically the same and fluctuated around 90% of the control. Thus, the presence of different concentrations of cobalt ferrite NPs in the samples does not affect their potential cytotoxicity. A slight decrease in viability relative to the control can presumably be explained by the fact that not all the surface of the tested samples was favorable for adhesion and proliferation; perhaps the edges of the sample pieces were not suitable for cells, but the main area was suitable.

Table 5. Proportion of viable mouse mesenchymal stem cells after incubation with samples for 24 h.

	Control	**PLA**	**PLA/$CoFe_2O_4$ (1 wt.%)**	**PLA/$CoFe_2O_4$ (5 wt.%)**	**PLA/$CoFe_2O_4$ (10 wt.%)**
Proportion of viable cells (mean value), %	100.0 ± 4.8	89.4 ± 9.6	93.5 ± 6.4	92.1 ± 11.1	87.0 ± 9.6

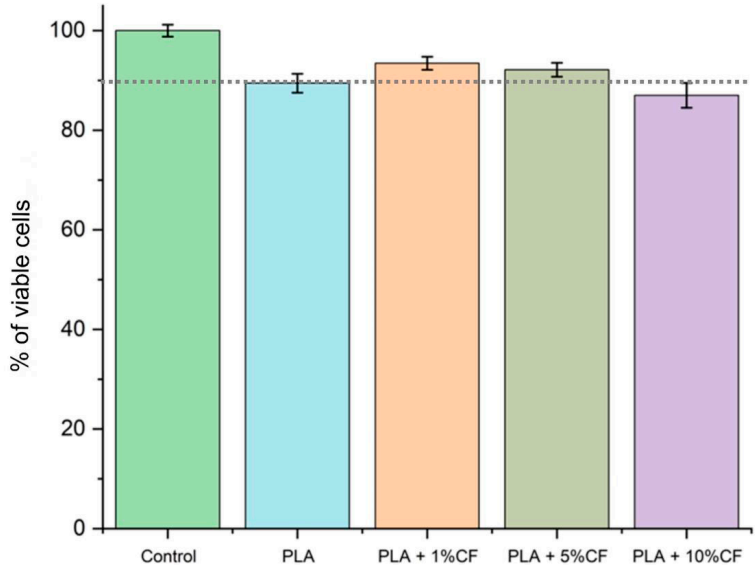

Figure 7. Proportion of viable cells in control wells and sample wells (n = 6).

4. Conclusions

Composite materials based on PLA with different contents of cobalt ferrite nanoparticles (1, 5, 10 wt.%) were obtained by extrusion. The degree of crystallinity of samples of pure PLA and PLA/$CoFe_2O_4$ (1 and 5 wt.%) did not exceed 8.1%. However, the value of the degree of crystallinity was 27.0% for a composite material with 10 wt.% $CoFe_2O_4$ NPs. It was noted that the degree of crystallinity of the polymer matrix increases with an increase in the amount of filler in the composite material. $CoFe_2O_4$ NPs acted as centers of crystallization and the formation of an additional rigid fixed phase, which determines the shape memory properties. The temperature at which the recoverable deformation

starts, decreased as the mass fraction of $CoFe_2O_4$ NPs in the PLA matrix increased, along with the glass transition temperature reduction. The value of reactive stresses during the implementation of the SME in the process of dynamic mechanical analysis increased with an increase in the mass fraction of NPs, and reached 3.6 MPa at the maximum concentration of the filler.

It was demonstrated that PLA and PLA/$CoFe_2O_4$ samples tested in vitro (1, 5, and 10 wt.%) do not have a significant cytotoxic effect and do not affect the proliferative activity of mouse mesenchymal stem cells. Such a material may be promising for the creation of adaptive medical devices, such as soft tissue fixators and "self-fitting" bone implants.

Supplementary Materials: The following supporting information can be downloaded at: https://www.mdpi.com/article/10.3390/jcs8020048/s1, Figure S1: Bright-field TEM image of NPs; Table S1: Main results of X-ray diffraction analysis of $CoFe_2O_4$ NPs; Figure S2: Diffractogram of cobalt ferrite MNPs powder; Figure S3: Magnetization curves of cobalt ferrite; Figure S4: Recovery strain curves for PLA and PLA/$CoFe_2O_4$ (1, 5, 10 wt.%) samples; Video S1: Shape recovery in HFAMF in the presence of mouse small intestine; Figure S5: Demonstration of SME in small intestine; Figure S6: Mesenchymal stem cells (*) at bottom of plate well and on surface of PLA sample; Figure S7: Mesenchymal stem cells (*) at bottom of plate well and on surface of PLA sample + 1% cobalt ferrite NPs.

Author Contributions: Conceptualization, M.A. and F.S.; methodology, F.S. and S.K.; validation, A.Z., A.N., S.V., E.P. and R.C.; formal analysis, A.Z., V.L. and R.C.; investigation, A.Z., A.N., V.L., I.B., P.K., M.Z. and E.P.; resources, A.Z., A.N., E.P. and S.K.; data curation, A.Z.; writing—original draft preparation, A.Z., A.N. and S.V.; writing—review and editing, I.B., S.K., R.C. and F.S.; visualization, A.Z., V.L. and P.K.; supervision, S.K., M.A. and F.S.; project administration, F.S.; funding acquisition, F.S. All authors have read and agreed to the published version of the manuscript.

Funding: This research was funded by the Russian Science Foundation (RSF), project No. 21-73-20205.

Institutional Review Board Statement: The in vivo studies presented in the manuscript "Impact of $CoFe_2O_4$ magnetic nanoparticles on the physical and mechanical properties and shape memory effect of polylactide" were performed using lab mice (8-week-old females Balb/c with weight 20 g). All procedures including the cell isolation and SME study on the mouse's small intestine was conducted with the approval of the Local Ethical Committee of N.N. Blokhin NMRC of Oncology. The work was conducted according to the Ethical Committee protocol (decision 2021-17 issued on 5 October 2021). The protocol is guided by the Decision N 81 of the European Economic Commission "On approval of rules of good laboratory practice of the Eurasian Economic Union in the sphere of circulation of medicines", issued on 3 November 2016, and Directive 2010/63/EU of the European Parliament and European Counsel issued on 22 September 2010 "On the protection of animals used in the laboratory research".

Data Availability Statement: The data presented in this study are available on request from the corresponding author.

Acknowledgments: The authors thank Sergey Zhirnov for sample preparation.

Conflicts of Interest: The authors declare no conflicts of interest.

References

1. Reddy, M.S.B.; Ponnamma, D.; Choudhary, R.; Sadasivuni, K.K. A comparative review of natural and synthetic biopolymer composite scaffolds. *Polymers* **2021**, *13*, 1105. [CrossRef] [PubMed]
2. Kumar, R.; Bairwa, K.N.; Reddy, D.R. Influence of addition of Al2O3 and SiC on tensile and flexural characteristics of epoxy/glass fiber hybrid polymer composite. *Mater. Today Proc.* **2023**. [CrossRef]
3. Tekay, E. Low-Voltage Triggered Electroactive and Heat-Responsive Thermoplastic Elastomer/Carbon Nanotube Polymer Blend Composites. *Mater. Today Commun.* **2023**, *35*, 106443. [CrossRef]
4. Tang, X.; Pionteck, J.; Pötschke, P. Improved piezoresistive sensing behavior of poly (vinylidene fluoride)/carbon black composites by blending with a second polymer. *Polymer* **2023**, *268*, 125702. [CrossRef]
5. Ismail, A.S.; Jawaid, M.; Hamid, N.H.; Yahaya, R.; Hassan, A.; Sarmin, S.N. Physical, structural and thermal properties of bio-phenolic/epoxy polymers blends. *Mater. Today Commun.* **2023**, *34*, 105455. [CrossRef]

6. Sun, L.; Huang, W.M.; Ding, Z.; Zhao, Y.; Wang, C.C.; Purnawali, H.; Tang, C. Stimulus-responsive shape memory materials: A review. *Mater. Des.* **2012**, *33*, 577–640. [CrossRef]
7. Rokaya, D.; Srimaneepong, V.; Sapkota, J.; Qin, J.; Siraleartmukul, K.; Siriwongrungson, V. Polymeric materials and films in dentistry: An overview. *J. Adv. Res.* **2018**, *14*, 25–34. [CrossRef]
8. Smith, K.E.; Garcia, M.; Dupont, K.M.; Higgs, G.B.; Gall, K.; Safranski, D.L. Shape-memory Polymers for Orthopaedic Soft-Tissue Repair. *Tech. Orthop.* **2017**, *32*, 141–148. [CrossRef]
9. Zhang, Q.; Zhao, Z.; Wu, D.; Chen, K.; Weng, S. Mechanics-guided design of inflatable heterogeneous shape memory polymer vascular stents. *Int. J. Mech. Sci.* **2023**, *254*, 108405. [CrossRef]
10. Masuda, T.; Miyazawa, K.; Ueda, N.; Hata, Y.; Kawai, T.; Goto, S. Development of an orthodontic elastic material using EMA-based resin combined with 1-butanol. *Dent. Mater. J.* **2011**, *30*, 664–671. [CrossRef] [PubMed]
11. Pietrzak, W.S.; Eppley, B.L.M. An experimental study of heat adaptation of bioabsorbable craniofacial meshes and plates. *J. Craniofac. Surg.* **2007**, *18*, 540–545. [CrossRef]
12. Stiller, A.M.; Usoro, J.O.; Lawson, J.; Araya, B.; González-González, M.A.; Danda, V.R.; Voit, W.E.; Black, B.J.; Pancrazio, J.J. Mechanically robust, softening shape memory polymer probes for intracortical recording. *Micromachines* **2020**, *11*, 619. [CrossRef]
13. Sánchez, C.P.; Jérôme, C.; Noels, L.; Vanderbemden, P. Review of Thermoresponsive Electroactive and Magnetoactive Shape Memory Polymer Nanocomposites. *ACS Omega* **2022**, *7*, 40701–40723. [CrossRef]
14. Wu, L.; Jin, C.; Sun, X. Synthesis, properties, and light-induced shape memory effect of multiblock polyesterurethanes containing biodegradable segments and pendant cinnamamide groups. *Biomacromolecules* **2011**, *12*, 235–241. [CrossRef]
15. Lendlein, A.; Jiang, H.; Jünger, O.; Langer, R. Light-induced shape-memory polymers. *Nature* **2005**, *434*, 879–882. [CrossRef]
16. Lee, K.M.; Koerner, H.; Vaia, R.A.; Bunning, T.J.; White, T.J. Light-activated shape memory of glassy, azobenzene liquid crystalline polymer networks. *Soft Matter* **2011**, *7*, 4318–4324. [CrossRef]
17. Ma, C.; Lu, W.; Yang, X.; He, J.; Le, X.; Wang, L.; Zhang, J.; Serpe, M.J.; Huang, Y.; Chen, T. Bioinspired anisotropic hydrogel actuators with on–off switchable and color-tunable fluorescence behaviors. *Adv. Funct. Mater.* **2018**, *28*, 1704568. [CrossRef]
18. Liu, T.; Huang, R.; Qi, X.; Dong, P.; Fu, Q. Facile preparation of rapidly electro-active shape memory thermoplastic polyurethane/polylactide blends via phase morphology control and incorporation of conductive fillers. *Polymer* **2017**, *114*, 28–35. [CrossRef]
19. Dong, Y.; Ni, Q.-Q.; Li, L.; Fu, Y. Novel vapor-grown carbon nanofiber/epoxy shape memory nanocomposites prepared via latex technology. *Mater. Lett.* **2014**, *132*, 206–209. [CrossRef]
20. Zeng, C.; Liu, L.; Bian, W.; Liu, Y.; Leng, J. 4D printed electro-induced continuous carbon fiber reinforced shape memory polymer composites with excellent bending resistance. *Compos. Part B Eng.* **2020**, *194*, 108034. [CrossRef]
21. Wang, L.; Razzaq, M.Y.; Rudolph, T.; Heuchel, M.; Nöchel, U.; Mansfeld, U.; Jiang, Y.; Gould, O.E.C.; Behl, M.; Kratz, K.; et al. Reprogrammable, magnetically controlled polymeric nanocomposite actuators. *Mater. Horiz.* **2018**, *5*, 861–867. [CrossRef]
22. Liu, H.; Wang, F.; Wu, W.; Dong, X.; Sang, L. 4D printing of mechanically robust PLA/TPU/Fe3O4 magneto-responsive shape memory polymers for smart structures. *Compos. Part B Eng.* **2023**, *248*, 110382. [CrossRef]
23. Gao, Y.; Zhu, G.; Xu, S.; Ma, T.; Nie, J. Biodegradable magnetic-sensitive shape memory poly (ε-caprolactone)/Fe_3O_4 nanocomposites. *J. Appl. Polym. Sci.* **2018**, *135*, 45652. [CrossRef]
24. Du, H.; Liu, X.; Yu, Y.; Xu, Y.; Wang, Y.; Liang, Z. Microwave-Induced Poly(ionic liquid)/Poly(vinyl alcohol) Shape Memory Composites. *Macromol. Chem. Phys.* **2016**, *217*, 2626–2634. [CrossRef]
25. Du, H.; Song, Z.; Wang, J.; Liang, Z.; Shen, Y.; You, F. Microwave-induced shape-memory effect of silicon carbide/poly(vinyl alcohol) composite. *Sens. Actuators A Phys.* **2015**, *228*, 1–8. [CrossRef]
26. Correia, C.O.; Caridade, S.G.; Mano, J.F. Chitosan membranes exhibiting shape memory capability by the action of controlled hydration. *Polymers* **2014**, *6*, 1178–1186. [CrossRef]
27. Yang, Y.; Terentjev, E.M.; Wei, Y.; Ji, Y. Solvent-assisted programming of flat polymer sheets into reconfigurable and self-healing 3D structures. *Nat. Commun.* **2018**, *9*, 1906. [CrossRef]
28. Bhargava, A.; Peng, K.; Stieg, J.; Mirzaeifar, R.; Shahab, S. Focused ultrasound actuation of shape memory polymers; acoustic-thermoelastic modeling and testing. *RSC Adv.* **2017**, *7*, 45452–45469. [CrossRef]
29. Li, G.; Yan, Q.; Xia, H.; Zhao, Y. Therapeutic-ultrasound-triggered shape memory of a melamine-enhanced poly(vinyl alcohol) physical hydrogel. *ACS Appl. Mater. Interfaces* **2015**, *7*, 12067–12073. [CrossRef]
30. Garces, I.T.; Aslanzadeh, S.; Boluk, Y.; Ayranci, C. Effect of Moisture on shape memory polyurethane polymers for extrusion-based additive manufacturing. *Materials* **2019**, *12*, 244. [CrossRef]
31. Li, S.-T.; Jin, X.-Z.; Shao, Y.-W.; Qi, X.-D.; Yang, J.-H.; Wang, Y. Gold nanoparticle/reduced graphene oxide hybrids for fast light-actuated shape memory polymers with enhanced photothermal conversion and mechanical stiffness. *Eur. Polym. J.* **2019**, *116*, 302–310. [CrossRef]
32. Xie, H.; Shao, J.; Ma, Y.; Wang, J.; Huang, H.; Yang, N.; Wang, H.; Ruan, C.; Luo, Y.; Wang, Q.-Q.; et al. Biodegradable near-infrared-photoresponsive shape memory implants based on black phosphorus nanofillers. *Biomaterials* **2018**, *164*, 11–21. [CrossRef]
33. Sun, L.; Wang, T.X.; Chen, H.M.; Salvekar, A.V.; Naveen, B.S.; Xu, Q.; Weng, Y.; Guo, X.; Chen, Y.; Huang, W.M. A brief review of the shape memory phenomena in polymers and their typical sensor applications. *Polymers* **2019**, *11*, 1049. [CrossRef] [PubMed]

34. Migneco, F.; Huang, Y.-C.; Birla, R.K.; Hollister, S.J. Poly(glycerol-dodecanoate), a biodegradable polyester for medical devices and tissue engineering scaffolds. *Biomaterials* **2009**, *30*, 6479–6484. [CrossRef]
35. Garle, A.; Kong, S.; Ojha, U.; Budhlall, B.M. Thermoresponsive semicrystalline poly(ε-caprolactone) networks: Exploiting cross-linking with cinnamoyl moieties to design polymers with tunable shape memory. *ACS Appl. Mater. Interfaces* **2012**, *4*, 645–657. [CrossRef]
36. Liu, Y.; Gall, K.; Dunn, M.L.; McCluskey, P. Thermomechanics of shape memory polymer nanocomposites. *Mech. Mater.* **2004**, *36*, 929–940. [CrossRef]
37. Wei, Z.G.; Sandstroröm, R.; Miyazaki, S. Shape-memory materials and hybrid composites for smart systems: Part I Shape-memory materials. *J. Mater. Sci.* **1998**, *33*, 3743–3762. [CrossRef]
38. García-García, G.; Lázaro-Callejón, M.; Fernández-Álvarez, F.; Iglesias, G.R.; Arias, J.L. (Magnetite/poly (ε-caprolactone))/chitosan (core/shell)/shell nanocomposites with potential applications in hyperthermia cancer therapy. *J. Magn. Magn. Mater.* **2023**, *588*, 171500. [CrossRef]
39. Montazersaheb, P.; Pishgahzadeh, E.; Jahani, V.B.; Farahzadi, R.; Montazersaheb, S. Magnetic nanoparticle-based hyperthermia: A prospect in cancer stem cell tracking and therapy. *Life Sci.* **2023**, *323*, 121714. [CrossRef]
40. Farzanegan, Z.; Tahmasbi, M. Evaluating the applications and effectiveness of magnetic nanoparticle-based hyperthermia for cancer treatment: A systematic review. *Appl. Radiat. Isot.* **2023**, *198*, 110873. [CrossRef]
41. Peiravi, M.; Eslami, H.; Ansari, M.; Zare-Zardini, H. Magnetic hyperthermia: Potentials and limitations. *J. Indian Chem. Soc.* **2022**, *99*, 100269. [CrossRef]
42. Zhang, F.; Wang, L.; Zheng, Z.; Liu, Y.; Leng, J. Magnetic programming of 4D printed shape memory composite structures. *Compos. Part A Appl. Sci. Manuf.* **2019**, *125*, 105571. [CrossRef]
43. Kim, Y.; Yuk, H.; Zhao, R.; Chester, S.A.; Zhao, X. Printing ferromagnetic domains for untethered fast-transforming soft materials. *Nature* **2018**, *558*, 274–279. [CrossRef]
44. Ma, C.; Wu, S.; Ze, Q.; Kuang, X.; Zhang, R.; Qi, H.J.; Zhao, R. Magnetic multimaterial printing for multimodal shape transformation with tunable properties and shiftable mechanical behaviors. *ACS Appl. Mater. Interfaces* **2020**, *13*, 12639–12648. [CrossRef]
45. Schmidt, A.M. Electromagnetic Activation of Shape Memory Polymer Networks Containing Magnetic Nanoparticles. *Macromol. Rapid Commun.* **2006**, *27*, 1168–1172. [CrossRef]
46. Scaffaro, R.; Lopresti, F.; Botta, L.; Rigogliuso, S.; Ghersi, G. Integration of PCL and PLA in a monolithic porous scaffold for interface tissue engineering. *J. Mech. Behav. Biomed. Mater.* **2016**, *63*, 303–313. [CrossRef] [PubMed]
47. Balla, E.; Daniilidis, V.; Karlioti, G.; Kalamas, T.; Stefanidou, M.; Bikiaris, N.D.; Vlchopoulos, A.; Koumentakou, I.; Bikiaris, D.N. Poly (lactic Acid): A versatile biobased polymer for the future with multifunctional properties—From monomer synthesis, polymerization techniques and molecular weight increase to PLA applications. *Polymers* **2021**, *13*, 1822. [CrossRef] [PubMed]
48. Pandey, A.; Singh, G.; Singh, S.; Jha, K.; Prakash, C. 3D printed biodegradable functional temperature-stimuli shape memory polymer for customized scaffoldings. *J. Mech. Behav. Biomed. Mater.* **2020**, *108*, 103781. [CrossRef]
49. da Silva, D.; Kaduri, M.; Poley, M.; Adir, O.; Krinsky, N.; Shainsky-Roitman, J.; Schroeder, A. Biocompatibility, biodegradation and excretion of polylactic acid (PLA) in medical implants and theranostic systems. *Chem. Eng. J.* **2018**, *340*, 9–14. [CrossRef] [PubMed]
50. Senatov, F.S.; Niaza, N.K.; Zadorozhnyy, M.Y.; Maksimkin, A.V.; Kaloshkin, S.D.; Estrin, Y.Z. Mechanical properties and shape memory effect of 3D-printed PLA-based porous scaffolds. *J. Mech. Behav. Biomed. Mater.* **2016**, *57*, 139–148. [CrossRef] [PubMed]
51. Kaseem, M.; Hamad, K.; Ur Rehman, Z. Review of recent advances in polylactic acid/TiO_2 composites. *Materials* **2019**, *12*, 3659. [CrossRef]
52. Kaseem, M.; Hamad, K.; Deri, F.; Ko, Y.G. A review on recent researches on polylactic acid/carbon nanotube composites. *Polym. Bull.* **2017**, *74*, 2921–2937. [CrossRef]
53. Tsai, P.A.; Chiu, W.M.; Lin, C.E.; Wu, J.H. Fabrication and characterization of PLA/SiO2/Al2O3 composites prepared by Sol-Gel process. *Polym. Plast. Technol. Eng.* **2013**, *52*, 1488–1495. [CrossRef]
54. Hamad, K.; Kaseem, M.; Deri, F. Preparation and characterization of binary and ternary blends with poly (lactic acid), polystyrene, and acrylonitrile-butadiene-styrene. *J. Biomater. Nanobiotechnol.* **2012**, *3*, 405–412. [CrossRef]
55. Zahn, D.; Landers, J.; Diegel, M.; Salamon, S.; Stihl, A.; Schacher, F.H.; Wende, H.; Dellith, J.; Dutz, S. Optimization of Magnetic Cobalt Ferrite Nanoparticles for Magnetic Heating Applications in Biomedical Technology. *Nanomaterials* **2023**, *13*, 1673. [CrossRef]
56. Amiri, M.; Salavati-Niasari, M.; Akbari, A. Magnetic nanocarriers: Evolution of spinel ferrites for medical applications. *Adv. Colloid Interface Sci.* **2019**, *265*, 29–44. [CrossRef]
57. Kharat, P.B.; Somvanshi, S.B.; Khirade, P.P.; Jadhav, K.M. Induction heating analysis of surface-functionalized nanoscale $CoFe_2O_4$ for magnetic fluid hyperthermia toward noninvasive cancer treatment. *ACS Omega* **2020**, *5*, 23378–23384. [CrossRef] [PubMed]
58. Elbeshir, E.I.A. Magnetic and thermal properties of CoFe2O4 nanoparticles for magnetic hyperthermia treatment. *Int. J. Adv. Appl. Scin.* **2018**, *5*, 34–36. [CrossRef]
59. Jia, W.; Qi, Y.; Hu, Z.; Xiong, Z.; Luo, Z.; Xiang, Z.; Hu, J.; Lu, W. Facile fabrication of monodisperse $CoFe_2O_4$ nanocrystals@dopamine@DOX hybrids for magnetic-responsive on-demand cancer theranostic applications. *Adv. Compos. Hybrid Mater.* **2021**, *4*, 989–1001. [CrossRef]

60. Ashour, A.; El-Batal, A.I.; Maksoud, M.A.; El-Sayyad, G.S.; Labib, S.; Abdeltwab, E.; El-Okr, M. Antimicrobial activity of metal-substituted cobalt ferrite nanoparticles synthesized by sol–gel technique. *Particuology* **2018**, *40*, 141–151. [CrossRef]
61. De, D.; Upadhyay, P.; Das, A.; Ghosh, A.; Adhikary, A.; Goswami, M.M. Studies on cancer cell death through delivery of dopamine as anti-cancer drug by a newly functionalized cobalt ferrite nano-carrier. *Colloids Surf. A Physicochem. Eng. Asp.* **2021**, *627*, 127202. [CrossRef]
62. Moeini, N.; Molaei, S.; Ghadermazi, M. Dysprosium (III) Supported on CoFe2O4 MNPs as a heterogeneous catalyst for the selective oxidation of sulfides and synthesis of symmetrical disulfides. *J. Mol. Struct.* **2021**, *1246*, 131071. [CrossRef]
63. Garanina, A.S.; Nikitin, A.A.; Abakumova, T.O.; Semkina, A.S.; Prelovskaya, A.O.; Naumenko, V.A.; Erofeev, A.S.; Gorelkin, P.V.; Majouga, A.G.; Abakumov, M.A.; et al. Cobalt ferrite nanoparticles for tumor therapy: Effective heating versus possible toxicity. *Nanomaterials* **2021**, *12*, 38. [CrossRef] [PubMed]
64. Vallabani, N.V.S.; Singh, S.; Karakoti, A.S. Magnetic nanoparticles: Current trends and future aspects in diagnostics and nanomedicine. *Curr. Drug Metab.* **2019**, *20*, 457–472. [CrossRef]
65. Kovaleva, P.A.; Pariy, I.O.; Chernozem, R.V.; Zadorozhnyy, M.Y.; Permyakova, E.S.; Kolesnikov, E.A.; Surmeneva, M.A.; Surmenev, R.A.; Senatov, F.S. Shape memory effect in hybrid polylactide-based polymer scaffolds functionalized with reduced graphene oxide for tissue engineering. *Eur. Polym. J.* **2022**, *181*, 111694. [CrossRef]
66. Senatov, F.S.; Zadorozhnyy, M.Y.; Niaza, K.V.; Medvedev, V.V.; Kaloshkin, S.D.; Anisimova, N.Y.; Kiselevskiy, M.V.; Yang, K.-C. Shape memory effect in 3D-printed scaffolds for self-fitting implants. *Eur. Polym. J.* **2017**, *93*, 222–231. [CrossRef]
67. Garanina, A.S.; Naumenko, V.A.; Nikitin, A.A.; Myrovali, E.; Petukhova, A.Y.; Klimyuk, S.V.; Nalench, Y.A.; Ilyasov, A.R.; Vodopyanov, S.S.; Erofeev, A.S.; et al. Temperature-controlled magnetic nanoparticles hyperthermia inhibits primary tumor growth and metastases dissemination. *Nanomed. Nanotechnol. Biol. Med.* **2020**, *25*, 102171. [CrossRef] [PubMed]
68. Battegazzore, D.; Bocchini, S.; Frache, A. Crystallization kinetics of poly(lactic acid)-talc composites. *Express Polym. Lett.* **2011**, *5*, 849–858. [CrossRef]
69. Krassikova, L.S.; Karshieva, S.S.; Cheglakov, I.B.; Belyavsky, A.V. Combined treatment, based on lysomustine administration with mesenchymal stem cells expressing cytosine deaminase therapy, leads to pronounced murine Lewis lung carcinoma growth inhibition. *J. Gene Med.* **2016**, *18*, 220–233. [CrossRef]
70. Vinosha, A.; Jeronsia, E.; Raja, K.; christina Fernandez, A.; Krishnan, S.; Das, J. Investigation of optical, electrical and magnetic properties of cobalt ferrite nanoparticles by naive co-precipitation technique. *Optik* **2016**, *127*, 9917–9925.
71. Karaagac, O.; Yildiz, B.B.; Köçkar, H. The influence of synthesis parameters on one-step synthesized superparamagnetic cobalt ferrite nanoparticles with high saturation magnetization. *J. Magn. Magn. Mater.* **2019**, *473*, 262–267. [CrossRef]
72. Li, J.; Zhao, X.; Ye, L.; Coates, P.; Caton-Rose, F. Multiple shape memory behavior of highly oriented long-chain-branched poly(lactic acid) and its recovery mechanism. *J. Biomed. Mater. Res. Part A* **2019**, *107*, 872–883. [CrossRef] [PubMed]
73. Nie, D.; Yin, X.; Cai, Z.; Wang, J. Effect of crystallization on shape memory effect of poly(lactic acid). *Polymers* **2022**, *14*, 1569. [CrossRef] [PubMed]
74. Ling, X. *Thermal and X-ray Analysis on the Origin of Double Melting Phenomena of Poly (L-Lactic Acid) Films*; The University of Tennessee: Knoxville, TN, USA, 2005.
75. Gong, X.; Cheng, C.; Tang, C.Y.; Law, W.; Lin, X.; Chen, Y.; Chen, L.; Tsui, G.C.P.; Rao, N. Crystallization behavior of polylactide matrix under the influence of nano-magnetite. *Polym. Eng. Sci.* **2019**, *59*, 608–615. [CrossRef]